Journal of
Materials Chemistry C

COMMUNICATION

View Article Online
View Journal

Cite this: DOI: 10.1039/c7tc00598a

Received 7th February 2017,
Accepted 20th March 2017

DOI: 10.1039/c7tc00598a

rsc.li/materials-c

Synthesis of formamidinium lead halide perovskite nanocrystals through solid–liquid–solid cation exchange†

K. Hills-Kimball, Y. Nagaoka, C. Cao, E. Chaykovsky and O. Chen *

Hybrid organic–inorganic perovskites (HOIPs) have emerged as promising materials for applications in solar energy harvesting as well as in optoelectronic devices. Here, we report the first demonstration of cation exchange on HOIP nanocrystals (NCs). In this reaction, methylammonium cations are replaced in methylammonium lead halide ($MAPbX_3$) NCs by formamidinium cations through a solid–liquid–solid cation exchange reaction. X-ray diffraction and optical characterizations allowed for the close monitoring of this process. Through this new type of cation-exchange reaction, formamidinium lead halide ($FAPbX_3$) NCs with various halide compositions were synthesized by altering the starting material. This allowed for the formation of $FAPbX_3$ HOIP NCs with a wide range of emissions spanning from 395 nm to 700 nm.

Introduction

Perovskite materials are characterized as possessing a chemical formula ABX_3, in which 'A' and 'B' signify two cations of differing size and charge that are each coordinated with anion 'X'. An ideal perovskite has a cubic framework in which eight corner-sharing BX_6 octahedra form a cuboctahedron that hosts an 'A' cation.[1] Among the perovskite material family, hybrid organic–inorganic perovskites (HOIP) represent a unique category, containing organic cations within the inorganic frame cages. In particular, colloidal halide-based HOIP (ABX_3, X = Cl^-, Br^-, and I^-) nanocrystals (NCs) have garnered a copious amount of research interest owing to their low-cost and facile processing, superior photoluminescence properties, and their potential in promising applications such as in light emitting devices (LED), solid state lighting and displays, photovoltaics, and lasing.[2–13] In recent years, significant efforts have been devoted to controlling the morphology, tuning the optoelectronic properties, and diversifying the organic and inorganic compositions of the halide-based HOIP NCs.[4,10,14–21] To this extent, post-synthetic chemical transformation through ion-exchange reactions has been recognized as a fast and powerful technique and has been successfully applied to various NC as well as thin film systems.[10,20,22–29] Owing to their unique defect-tolerant photophysical properties, perovskite materials after ion-exchanges typically preserve their crystal structures and optical properties, and therefore yield high performances in their optoelectronic applications.[13,14,19] However, to date, only anion-exchange reactions tuning the halide compositions in perovskite NCs have been reported.[10,20,22,23,28] To our best knowledge, a cation exchange reaction in HOIP NCs has not yet been demonstrated.

In this work, we introduce a synthesis of formamidinium lead halide ($FAPbX_3$) colloidal HOIP NCs through the first demonstrated *in situ* solid–liquid–solid cation exchange reaction from pre-synthesized methylammonium lead halide ($MAPbX_3$) NCs (Scheme 1). Detailed analyses using various characterization tools confirmed the completion of the replacement of MA^+ with FA^+ cations within the perovskite crystal structure. In addition, the obtained FA-based HOIP NCs preserved a cubic crystal structure and high photoluminescence quantum yields (PL QYs) of up to 69%. We showed that this solid–liquid–solid cation exchange reaction can be generalized for synthesizing $FAPbX_3$ HOIP NCs with various mixed halide compositions of the formula $FAPbBr_xCl_{(3-x)}$ and $FAPbBr_xI_{(3-x)}$. The emission peaks of the resultant FA-based HOIP NCs span the entire visible spectrum. We anticipate that this novel *in situ* solid–liquid–solid organic cation exchange method will be useful in further development of

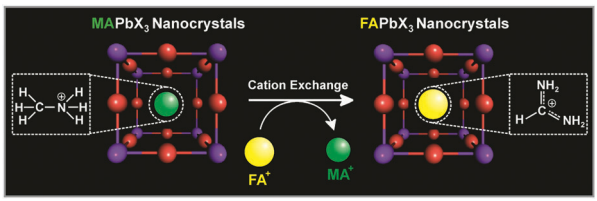

Scheme 1 Schematic of the solid–liquid–solid cation exchange within the cubic perovskite crystal structure from $MAPbX_3$ NCs to $FAPbX_3$ NCs.

Department of Chemistry, Brown University, Providence, RI 02912, USA.
E-mail: ouchen@brown.edu

† Electronic supplementary information (ESI) available. See DOI: 10.1039/c7tc00598a

new perovskite materials with targeted compositions for a multitude of applications.

Results and discussion

The starting $MAPbBr_3$ NCs were synthesized using a modified literature procedure.[4] The FA^+ cation exchange reaction was executed by adding solid formamidinium acetate (FA(ac)) to a toluene solution of $MAPbBr_3$ NCs. The FA(ac) is minimally soluble in toluene, which allowed for the cation exchange to slowly proceed while maintaining particle stability.

The cation exchange reaction was monitored using UV-Vis absorption and photoluminescence (PL) spectroscopies. Fig. 1A and B shows the evolution of the absorption and PL emission spectra throughout the reaction. Both the absorption spectral features and PL peak continuously shifted to a longer wavelength region. Specifically, the center of the PL peak shifted from 515 nm for the initial $MAPbBr_3$ NCs and stopped at 531 nm (Fig. 1B, C and Fig. S1, ESI†). No further peak red-shifting was observed with prolonged reaction time, indicating the completion of the FA^+ cation exchange reaction. This PL peak shift corresponded to ~73 meV, comparable to the band-gap difference of ~80 meV between $MAPbBr_3$ (2.34 eV) and $FAPbBr_3$ (2.26 eV) perovskites in bulk states.[30,31] Interestingly, the PL peak width decreased monotonically during the entire reaction. The full width at half maximum (FWHM) of the PL peak decreased from 122 meV (~26 nm) to 88 meV (~20 nm) as shown in Fig. 1B and C, suggesting a good particle size and shape distribution of the final $FAPbBr_3$ NCs.[32] The PL QY measurements showed that during the exchange reaction, the PL QY increased slightly and then decreased (Fig. S2, ESI†). The Final PL QY of $FAPbBr_3$ NCs was measured as 69%, which was comparable to that of the starting $MAPbBr_3$ NCs (PL QY of 72%). Preservation of a high PL QY is consistent with previous observations for anion-exchange reactions in $CsPbX_3$ systems as well as the high defect-tolerant photophysics property of perovskite materials.[22,23,33,34]

In addition to the change in band-gap structure, the overall increase in lifetime between $MAPbBr_3$ and $FAPbBr_3$ has also been reported on the bulk scale, which is afforded from the ability of the FA^+ cation to hold polarization longer than the MA^+ cation.[30,35] Within the perovskite structure, the FA^+ cation is capable of forming four short hydrogen bonds with the inorganic framework compared to the three formed by the MA^+ cation. This allows the FA^+ cation to generate a stronger interaction with the inorganic sublattice and in turn, allows for longer photo-carrier lifetimes.[30,35] To monitor the carrier decay dynamic changes during the FA^+ cation exchange reaction, ensemble PL lifetime decays were measured and a trend of increasing lifetime was observed (Fig. 1D). In total, $FAPbBr_3$ particles displayed about a four-fold longer photoexcited carrier lifetime than their MA^+ counterparts (10.2 ns *vs.* 35.9 ns), which is consistent with the lifetime increase of the bulk perovskite materials.[35] Each lifetime decay curve was fitted using a biexponential function, and it was observed that the shorter component shortened over the course of the reaction while the longer component simultaneously lengthened (Table S1, ESI†). The longer component also accounted for an increased contribution to the fitting function, which resulted in an increase of the overall photo-excited carrier lifetime from 10.2 ns to 35.9 ns (Table S1, ESI†). We speculate that the behaviour of the shorter lifetime component was due to the increased number of trap states that occurred as a consequence of the large organic cation (*i.e.*, FA^+) exchange and travel inside of the perovskite crystalline lattices. This behaviour was counteracted by the intrinsically prolonged lifetime of the $FAPbBr_3$ perovskites as compared to the $MAPbBr_3$ counterparts.[35] Taken together, the results shown here suggest that the observed optical property change is an outcome of replacing the MA^+ cation with the FA^+ cation inside the $MAPbBr_3$ HOIP NCs.

To further characterize the cation exchange reaction, powder X-ray diffraction (XRD) measurements were carried out to monitor the detailed crystal structure and lattice parameter evolutions over the entire reaction. However, initial XRD sample preparation failed due to the dissolution of HOIP NCs during the solvent drying process. During evaporation, there is an increased concentration of polar *N*,*N*-dimethylformamide (DMF) due to its higher boiling point (b.p. 153 °C) than that of toluene (b.p. 113 °C). As a result, the higher polarity environment can dissolve the HOIP NCs into their ionic forms.[4,36] This observation is consistent with other reports of HOIP XRD preparations.[36] In order to preserve the HOIP NCs' morphology for the XRD measurements, we found that it was effective to add a higher b.p. solvent (*i.e.*, mesitylene, b.p. 167 °C) to stabilize the HOIP NCs during the solvent evaporation. Following this modified sample preparation method (ESI†), a series of XRD spectra for the samples collected during the FA^+ cation exchange reaction was measured (Fig. 2A and B). XRD data showed that the initial $MAPbBr_3$ NCs exhibit a cubic crystal structure (space group: $pm\bar{3}m$) with a measured lattice constant of 5.91 Å, in good agreement with the previously reported value (Fig. 2A, B and Table S2, ESI†).[37,38] During the cation exchange, the perovskite NCs maintained a cubic crystal structure, while all the diffraction peaks shifted to smaller angles (Fig. 2A and B). The calculated lattice constant continuously increased from 5.91 Å to 6.01 Å (Table S2, ESI†). This change of the lattice constant corresponds

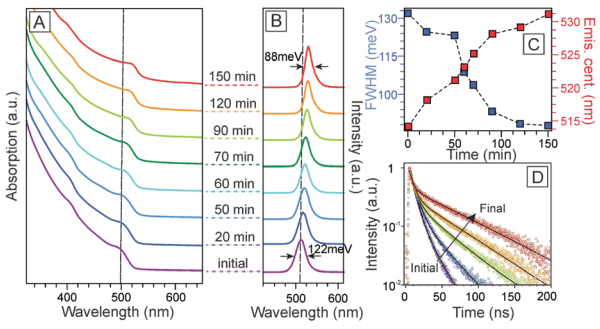

Fig. 1 Evolution of optical properties of HOIP NCs during the FA^+ cation exchange reaction. (A) Absorption spectra. (B) PL spectra. (C) PL peak position (red square) and FWHM (blue square) as a function of reaction time. (D) Evolution of the ensemble PL lifetime decay curves.

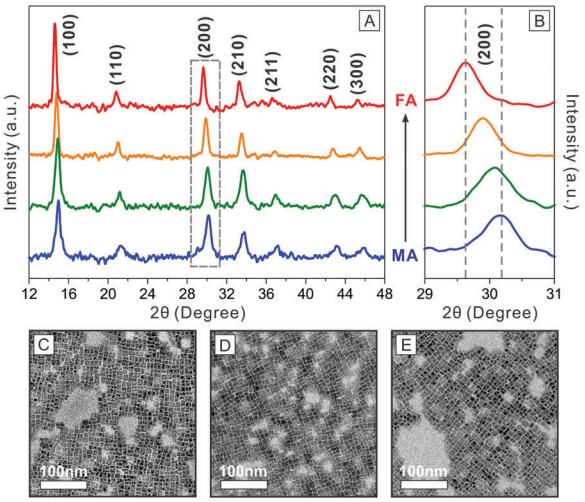

Fig. 2 Structural and morphology evolution of the HOIP NCs during the FA^+ cation exchange process. (A) XRD spectra. (B) Zoomed in XRD spectra of the rectangular area labelled in (A) for a clear visualization of the (200) peak shifting. (C–E) TEM images of (C) the initial $MAPbBr_3$ NCs, (D) the $FA_xMA_{(1-x)}PbBr_3$ NCs taken at 60 min during the cation exchange reaction, (E) the final $FAPbBr_3$ NCs.

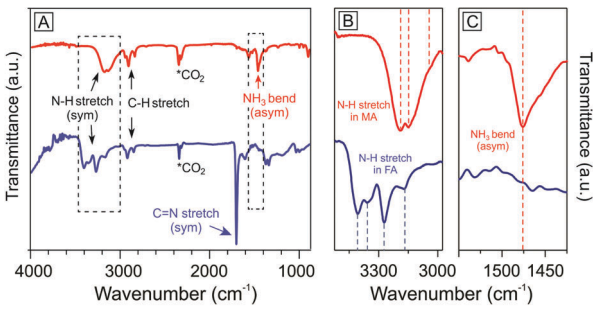

Fig. 3 (A) FTIR spectra of the initial $MAPbBr_3$ HOIP NCs (red) and final $FAPbBr_3$ NCs (blue). (B and C) The zoomed in FTIR spectra of the two rectangular areas (dashed line) labelled in (A). These areas clearly depict the IR feature difference between the MA^+ and FA^+ cations.

to a unit cell volume expansion of 5.2%, which matches the volume expansion from the $MAPbBr_3$ to $FAPbBr_3$ in the bulk states induced by the ionic radius difference of MA^+ (2.17 Å) and FA^+ (2.53 Å) cations.[9,31,39] The obtained lattice constant of 6.01 Å matched well with the reported value of 6.00 Å for $FAPbBr_3$ NCs, indicating a complete cation exchange.[3] In addition, the mean crystallite size calculated from the XRD peaks based on the Scherrer equation was maintained at ~17 nm throughout the reaction. This crystallite size was slightly larger than the NC size (cubic edge length of ~10 nm) determined by the transmission electron microscopy (TEM) measurements (Fig. 2C–E) and was likely due to some degree of NC fusion during the XRD sample preparation process. Moreover, we found that the (200) Bragg diffraction peak remained as a singular peak, differing from the emergence of two peaks as observed in gas-solid phase FA^+ cation exchanges in the bulk state.[26] This observation strongly suggested that our cation exchange happened *via* a molecular diffused alloying process (*e.g.*, vacancy-assisted), rather than through a segmented hetero-structure formation process.[24,40,41]

TEM was used to characterize the morphology of the HOIP NCs during the cation exchange reaction. Fig. 2C–E shows that the NCs' size, shape, and size distribution were retained throughout the reaction. The initial $MAPbBr_3$ NCs exhibited a cubic shape with an average edge length of 9.7 ± 1.0 nm (Fig. 2C), while the final $FAPbBr_3$ perovskite NCs showed a slightly increased edge length of 10.2 ± 1.1 nm without altering the cubic NC shape (Fig. 2E). TEM measurements showed a high consistency with the optical and XRD characterizations, further supporting that the observed optical and crystal lattice changes were due to the cation replacement and not through morphological or size variations of the NCs.

Accompanying the changes in band-gap structures and lattice parameters as a result of the cation exchange, Fourier transform infrared spectroscopy (FTIR) was employed to further identify the chemical identities within the perovskite crystal structures before and after the reaction. The FTIR spectrum for the initial $MAPbBr_3$ NC sample showed IR peaks at 3189 cm^{-1}, 3148 cm^{-1} and a shoulder at 3042 cm^{-1}, which can be assigned to the splitted N–H symmetric stretching mode of the MA^+ cation (Fig. 3A and B).[42] Additionally, the characteristic NH_3 asymmetric bending mode appeared at 1472 cm^{-1} for the $MAPbBr_3$ sample (Fig. 3A and C). These IR features signified the presence of organic MA^+ cations inside the inorganic perovskite framework. After the cation exchange reaction, the FTIR spectrum clearly showed different vibrational features (Fig. 3). In the high wavenumber region, quadruple IR bands showed up at 3407 cm^{-1}, 3359 cm^{-1}, 3272 cm^{-1}, and 3171 cm^{-1}, all of which belonged to N–H stretching vibrations for the FA^+ cations (Fig. 3A and B).[27] The observed quartet splitting is most likely caused by the four-short hydrogen bonds (N–H···Br) formed between the FA^+ and Br^- ions of the inorganic perovskite sublattice within the crystal.[27,42] Moreover, the emergence of a strong band at 1712 cm^{-1} unambiguously proved the presence of FA^+ cation with its strong C=N symmetric stretching (Fig. 3A).[27] Furthermore, the NH_3 asymmetric bending peak (1472 cm^{-1}) wholly disappeared in the FTIR spectrum of the final sample (Fig. 3C). In total, the emergence of the new IR bands together with the total disappearance of the original MA^+ vibrational features strongly support our conclusion of a complete replacement of MA^+ with FA^+ cations in the HOIP NCs.

Additionally, it is worth mentioning that the cation exchange reaction presented here was more than two orders of magnitude slower than the previously reported liquid phase halide anion exchange processes and gas-solid cation exchange (150 min *vs.* <1 min).[22,23] This could be attributed to the low solubility of ionic solid FA(ac) in nonpolar solvents (*i.e.*, toluene) used for the reaction. We speculate that the presence of extra oleic acid from the $MAPbBr_3$ NC synthesis solution played a role as a chelating agent, granting FA^+ cations a minimal solubility in toluene through formations of hydrogen bonding and/or amide bonds, and allowing for FA^+ transport to the NCs' surface.[43] The high lattice energy of $FAPbBr_3$ crystals as compared to their MA counterparts thermodynamically drives the cation exchange reaction towards completion.[44] However, the slow exchange

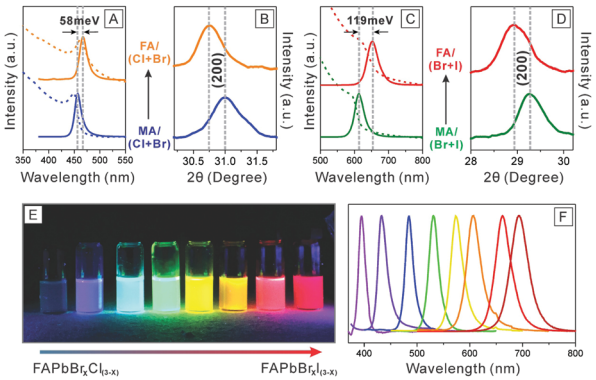

Fig. 4 (A and B) Optical and structural evolution of mixed Cl^-/Br^- HOIP NCs. (A) Absorption (dotted line) and PL spectra (solid line) of the initial $MAPbBr_xCl_{3-x}$ NCs (blue) and the final $FAPbBr_xCl_{3-x}$ NCs (orange). (B) Zoomed-in XRD spectra of the (200) diffraction peak area. (C and D) Optical and structural evolution of mixed I^-/Br^- HOIP NCs. (C) Absorption (dotted line) and PL spectra (solid line) of the initial $MAPbBr_xI_{3-x}$ NCs (green) and the final $FAPbBr_xI_{3-x}$ NCs (red). (D) Zoomed-in XRD spectra of the (200) diffraction peak area. (E) A photograph of $FAPbX_3$ HOIP NCs under UV illumination. (F) PL spectra of the synthesized $FAPbX_3$ HOIP NCs with different halide compositions.

kinetics presented here allow for reaction termination at fine-controlled intermediate stages and subsequent harvesting of HOIP NCs with mixed organic cation (*i.e.*, MA^+ and FA^+) compositions.

Finally, this solid–liquid–solid cation exchange reaction using FA(ac) has been generalized for making FA-based HOIP NCs with mixed halide compositions. Detailed analyses revealed a general trend, in which a smaller PL band-gap shift was observed while increasing the proportion of Cl^- in $MAPbBr_xCl_{3-x}$ NCs, in contrast to the trend observed when increasing the proportion of I^- in $MAPbBr_xI_{3-x}$ NCs, where larger band-gap shifts were observed after the FA^+ cation exchange reaction. Fig. 4A–D show absorption and PL spectra and the corresponding shifts in (200) XRD peak positions for two mixed halide NCs ($MAPbBr_{1.05}Cl_{1.95}$ and $MAPbBr_{1.2}I_{1.8}$) before and after the FA^+ cation exchange reactions. The XRD measurements (Fig. 4B, D and Fig. S3, S4, Tables S4, S5, ESI†) showed volume expansions of 2.6% and 4.5%, respectively, for the $FAPbBr_{1.05}Cl_{1.95}$ and $FAPbBr_{1.2}I_{1.8}$ NC samples compared to their initial MA counterparts, and confirmed the completion of the cation exchange (see detailed analysis in ESI†). The PL peak shifted from 457 nm to 467 nm for the $MAPbBr_{1.05}Cl_{1.95}$ NC sample, corresponding to a band-gap energy decrease of 58 meV. In contrast, the PL peak shifted from 612 nm to 650 nm for the $MAPbBr_{1.2}I_{1.8}$ NC sample, corresponding to a band-gap energy decrease of 119 meV. It is noteworthy that as the Cl^- or I^- halide composition was increased, the final FA-based HOIP NCs showed decreased colloidal stabilities. Further stability improvements, such as encapsulation or templating, need to be made for practical applications. Fig. 4E and F show the PL spectra for a range of $FAPbX_3$ NCs synthesized using initial $MAPbX_3$ NCs with various halide compositions. The emission color of the synthesized FA-based HOIP NCs covers the entire visible region from 395–700 nm (Fig. 4F).

Conclusions

In conclusion, we reported, for the first time, a synthesis of $FAPbX_3$ HOIP NCs through an *in situ* solid–liquid–solid cation exchange reaction. In the reaction, ionic solid FA(ac) which possessed a minimal solubility in toluene, was used as an FA^+ source allowing for a slow and controllable exchange between MA^+ and FA^+ cations. We demonstrated that the MA^+ cations could be fully replaced by FA^+ cations to generate $FAPbX_3$ HOIP NCs while preserving the size, shape and crystal structure of the starting $MAPbX_3$ HOIP NCs. The resulting $FAPbBr_3$ HOIP NCs exhibited a narrow emission profile (FWHM ~88 meV), a prolonged ensemble PL lifetime (~35.9 ns) and a high PL QY of up to 69%. Furthermore, we showed that this *in situ* solid–liquid–solid cation exchange procedure can be generalized for synthesizing a range of $FAPbX_3$ perovskites NCs with mixed halide compositions through alterations of the starting $MAPbX_3$ material. This work paves the way towards a variety of cation exchange reactions for synthesizing various HOIP NCs, which can be further applied in applications such as LED, displays, and lasing.

Acknowledgements

O. C. acknowledges the support from the Brown University startup fund and the Salomon award fund. K. H. is supported by the GAANN research fellowship. The TEM and XRD measurements were performed at the Nano Tools Facility and the Electron Microscopy Facility in the Institute for Molecular and Nanoscale Innovation (IMNI) at the Brown University.

Notes and references

1 A. R. West, *Solid state chemistry and its applications*, John Wiley & Sons, USA, 2007.
2 A. Nurmikko, *Nat. Nanotechnol.*, 2015, **10**, 1001–1004.
3 L. Protesescu, S. Yakunin, M. I. Bodnarchuk, F. Bertolotti, N. Masciocchi, A. Guagliardi and M. V. Kovalenko, *J. Am. Chem. Soc.*, 2016, **138**, 14202–14205.
4 F. Zhang, H. Zhong, C. Chen, X. G. Wu, X. Hu, H. Huang, H. Junbo, Z. Bingsuo and Y. Dong, *ACS Nano*, 2015, **9**, 4533–4542.
5 D. M. Jang, D. H. Kim, K. Park, J. Park, J. W. Lee and J. K. Song, *J. Mater. Chem. C*, 2016, **4**, 10625–10629.
6 O. Vybornyi, S. Yakunin and M. V. Kovalenko, *Nanoscale*, 2016, **8**, 6278–6283.
7 Y. Fu, H. Zhu, A. W. Schrader, D. Liang, Q. Ding, P. Joshi, L. Hwang, X.-Y. Zhu and S. Jin, *Nano Lett.*, 2016, **16**, 1000–1008.
8 H. Huang, F. Zhao, L. Liu, F. Zhang, X.-G. Wu, L. Shi, B. Zou, Q. Pe and H. Zhong, *ACS Appl. Mater. Interfaces*, 2015, **7**, 28128–28133.
9 Q. Chen, N. D. Marco, Y. Yang, T.-B. Song, C.-C. Chen, H. Zhao, Z. Hong, H. Zhou and Y. Yang, *Nano Today*, 2015, **10**, 355–396.

10 A. B. Wong, M. Lai, S. W. Eaton, Y. Yu, E. Lin, L. Dou, A. Fu and P. Yang, *Nano Lett.*, 2015, **15**, 5519–5524.
11 Z. Ning, X. Gong, R. Comin, G. Walters, F. Fan, O. Voznyy, E. Yassitepe, A. Buin, S. Hoogland and E. H. Sargent, *Nature*, 2015, **523**, 324–328.
12 H. Zhu, Y. Fu, F. Meng, X. Wu, Z. Gong, Q. Ding, M. Gustafsson, M. T. Trinh, S. Jin and X. Zhu, *Nat. Mater.*, 2015, **14**, 636–642.
13 H. Zhu, M. T. Trinh, J. Wang, Y. Fu, P. P. Joshi, K. Miyata, S. Jin and X. Y. Zhu, *Adv. Mater.*, 2017, **29**, 1603072.
14 L. Protesescu, S. Yakunin, M. I. Bodnarchuk, F. Krieg, R. Caputo, C. H. Hendon, R. X. Yang, A. Walsh and M. V. Kovalenko, *Nano Lett.*, 2015, **15**, 3692–3696.
15 M. Mittal, A. Jana, S. Sarkar, P. Mahadevan and S. Sapra, *J. Phys. Chem. Lett.*, 2016, **7**, 3270–3277.
16 L. N. Quan, M. Yuan, R. Comin, O. Voznyy, E. M. Beauregard, S. Hoogland, A. Buin, A. R. Kirmani, K. Zhao and A. Amassian, *J. Am. Chem. Soc.*, 2016, **138**, 2649–2655.
17 F. Zhu, L. Men, Y. Guo, Q. Zhu, U. Bhattacharjee, P. M. Goodwin, J. W. Petrich, E. A. Smith and J. Vela, *ACS Nano*, 2015, **9**, 2948–2959.
18 M. C. Weidman, M. Seitz, S. D. Stranks and W. A. Tisdale, *ACS Nano*, 2016, **10**, 7830–7839.
19 M. Leng, Z. Chen, Y. Yang, Z. Li, K. Zeng, K. Li, G. Niu, Y. He, Q. Zhou and J. Tang, *Angew. Chem., Int. Ed.*, 2016, **55**, 15012–15016.
20 D. M. Jang, K. Park, D. H. Kim, J. Park, F. Shojaei, H. S. Kang, J.-P. Ahn, J. W. Lee and J. K. Song, *Nano Lett.*, 2015, **15**, 5191–5199.
21 J. Dai, Y. Fu, L. H. Manger, M. T. Rea, L. Hwang, R. H. Goldsmith and S. Jin, *J. Phys. Chem. Lett.*, 2016, **7**, 5036–5043.
22 Q. A. Akkerman, V. D'Innocenzo, S. Accornero, A. Scarpellini, A. Petrozza, M. Prato and L. Manna, *J. Am. Chem. Soc.*, 2015, **137**, 10276–10281.
23 G. Nedelcu, L. Protesescu, S. Yakunin, M. I. Bodnarchuk, M. J. Grotevent and M. V. Kovalenko, *Nano Lett.*, 2015, **15**, 5635–5640.
24 W. S. Yang, J. H. Noh, N. J. Jeon, Y. C. Kim, S. Ryu, J. Seo and S. I. Seok, *Science*, 2015, **348**, 1234–1237.
25 G. E. Eperon, C. E. Beck and H. J. Snaith, *Mater. Horiz.*, 2016, **3**, 63–71.
26 Y. Zhou, M. Yang, S. Pang, K. Zhu and N. P. Padture, *J. Am. Chem. Soc.*, 2016, **138**, 5535–5538.
27 Z. Zhou, S. Pang, F. Ji, B. Zhang and G. Cui, *Chem. Commun.*, 2016, **52**, 3828–3831.
28 C. Guhrenz, A. Benad, C. Ziegler, D. Haubold, N. Gaponik and A. Eychmüller, *Chem. Mater.*, 2016, **28**, 9033–9040.
29 N. Pellet, J. Teuscher, J. Maier and M. Grätzel, *Chem. Mater.*, 2015, **27**, 2181–2188.
30 C. Motta, F. El-Mellouhi and S. Sanvito, *Phys. Rev. B: Condens. Matter Mater. Phys.*, 2016, **93**, 235412.
31 F. C. Hanusch, E. Wiesenmayer, E. Mankel, A. Binek, P. Angloher, C. Fraunhofer, N. Giesbrecht, J. M. Feckl, W. Jaegermann, D. Johrendt, T. Bein and P. Docampo, *J. Phys. Chem. Lett.*, 2014, **5**, 2791–2795.
32 O. Chen, J. Zhao, V. P. Chauhan, J. Cui, C. Wong, D. K. Harris, H. Wei, H.-S. Han, D. Fukumura, R. K. Jain and M. G. Bawendi, *Nat. Mater.*, 2013, **12**, 445–451.
33 A. Zakutayev, C. M. Caskey, A. N. Fioretti, D. S. Ginley, J. Vidal, V. Stevanovic, E. Tea and S. Lany, *J. Phys. Chem. Lett.*, 2014, **5**, 1117–1125.
34 R. E. Brandt, V. Stevanovic, D. S. Ginley and T. Buonassisi, *MRS Commun.*, 2015, **5**, 265–275.
35 A. A. Zhumekeno, M. I. Saidaminov, M. A. Haque, E. Alarousu, S. P. Sarmah, B. Murali, I. Dursun, X.-H. Miao, A. L. Abdelhady, T. Wu, O. F. Mohammed and O. M. Bakr, *ACS Energy Lett.*, 2016, **1**, 32–37.
36 H. Huang, A. S. Susha, S. V. Kershaw, T. F. Hung and A. L. Rogach, *Adv. Sci.*, 2015, **2**, 1500194.
37 L. C. Schmidt, A. Pertegás, S. González-Carrero, O. Malinkiewicz, S. Agouram, G. M. Espallargas, H. J. Bolink, R. E. Galian and J. Pérez-Prieto, *J. Am. Chem. Soc.*, 2014, **136**, 850–853.
38 P. Tyagi, S. M. Arveson and W. A. Tisdale, *J. Phys. Chem. Lett.*, 2015, **6**, 1911–1916.
39 G. Nagabhushana, R. Shivaramaiah and A. Navrotsky, *Proc. Natl. Acad. Sci. U. S. A.*, 2016, **113**, 7717–7721.
40 J. Haruyama, K. Sodeyama, L. Han and Y. Tateyama, *J. Am. Chem. Soc.*, 2015, **137**, 10048–10051.
41 L. De Trizio and L. Manna, *Chem. Rev.*, 2016, **116**, 10852–10887.
42 L.-Q. Xie, T.-Y. Zhang, L. Chen, N. Guo, Y. Wang, G.-K. Liu, J.-R. Wang, J.-Z. Zhou, J.-W. Yan, Y.-X. Zhao, B.-W. Mao and Z.-Q. Tiana, *Phys. Chem. Chem. Phys.*, 2016, **18**, 18112–18118.
43 T. Maugard, M. RemaudSimeon, D. Petre and P. Monsan, *Tetrahedron*, 1997, **53**, 7629–7634.
44 W. Li, J. Fan, J. Li, G. Niu, Y. Mai and L. Wang, *ACS Appl. Mater. Interfaces*, 2016, **8**, 30107–30115.